PERGAMON

International Journal of Heat and Mass Transfer 44 (2001) 2933–2947

International Journal of HEAT and MASS TRANSFER

www.elsevier.com/locate/ijhmt

Isothermal surface production and regulation for high heat flux applications utilizing porous inserts

K. Khanafer, K. Vafai *

Department of Mechanical Engineering, Ohio State University, Columbus, OH 43210, USA

Received 26 October 1999; received in revised form 9 October 2000

Abstract

The present work deals with an innovative way for producing and regulating an isothermal surface in high heat flux applications. This is achieved through the use of two fundamental configurations employing variable area channels. The flow field is modeled using the generalized formulation of the momentum equation and the energy equation is modeled based on one and two equation models. A comprehensive analysis of the influence of the inclination angle in producing flow area variations and its influence in creating an isothermal surface in the presence of an imposed high heat flux is presented. An isothermal surface along the bottom wall of a variable area channel configuration subjected to a high heat flux is produced for various controlling parameters and is presented graphically. The results presented in this work constitute an innovative way of producing and regulating isothermal surfaces in the presence of an imposed high heat flux.

Keywords: Isothermal surface production; High heat flux; Porous medium

1. Introduction

Thermal control of electronic equipment and devices has received considerable attention by investigators in the past decades. In a number of applications related to the thermal control of electronic components, a primary requirement is the maintenance of relatively constant component temperature equal to or below a maximum operating temperature. This constant component temperature plays a significant role in the performance of the electronic equipment. Studies have shown that a significant change in the design temperature can lead to an appreciable reduction in the reliability of the electronic components. Different techniques have been used in the past to obtain a well-controlled thermal environment including the traditional methods of natural and forced convective cooling. One of the promising techniques is the application of a porous material, due to its very large surface area per unit volume, in enhancing the heat transfer process.

Transport phenomena through porous media has been of continuing interest due to its presence in diverse engineering applications. Such applications include the geothermal energy systems, building thermal insulation, heat exchangers, solid-matrix heat exchangers, enhanced oil recovery, and nuclear waste disposal. Porous media is also utilized in applications such as fixed-bed nuclear propulsion systems, industrial furnaces, combustors, cooling of electronic equipment, and spacecraft thermal management systems.

The problem of forced convective fluid flow through a confined porous media has been studied extensively in the literature. Vafai and Huang [1] analyzed the effect of forced convection over intermittently emplaced porous cavities. They concluded that porous cavities can indeed be used in regulating skin friction and enhancing the heat transfer rate. Vafai and Kim [2] investigated the thermal performance for a composite porous medium-fluid system. Their results showed that the porous

* Corresponding author. Present address: Department of Mechanical Engineering, University of California, Riverside, A363 Bourns Hall, Riverside, CA 92521-0425, USA. Tel.: +1-909-787-2135; fax: +1-909-787-2899.

E-mail address: vafai@engr.ucr.edu (K. Vafai).

0017-9310/01/$ - see front matter
PII: S0017-9310(00)00336-7

Nomenclature

A	width of the enclosure
AR	aspect ratio, L/H
Da	Darcy number, K/H^2
d_p	particle diameter
F	geometry function
g	gravitational acceleration
H	minimum porous thickness
k_e	effective thermal conductivity of the porous medium
L	flow length, $A-2t_w$
P	fluid pressure
Pr	Prandtl number, v_e/α_e
Re	Reynolds number, V_oH/v_e
T	temperature
T_i	inlet port temperature
ΔT	temperature difference
t	time
u	velocity in x-direction
U	dimensionless x-component of velocity, u/V_o
v	velocity in y-direction
V	dimensionless y-component of velocity, v/V_o
V_o	inlet port velocity
t_w	enclosure wall thickness
w_i	enclosure inlet width
w_o	enclosure outlet width
x,y	Cartesian coordinates
X,Y	dimensionless Cartesian coordinates,$(x,y)/H$

Greek symbols

α_e	effective thermal diffusivity of porous medium
ρ	density
ε	porosity
φ	inclination angle
K	permeability of the porous medium
μ_e	effective dynamic viscosity
v_e	effective kinematic viscosity, μ_e/ρ
θ	dimensionless temperature, $(T-T_i)/\Delta T$
Θ	dimensionless solid temperature, $(T_s-T_i)/\Delta T$
ψ	stream function
Ψ	dimensionless stream function, ψ/HV_o
Ω	dimensional vorticity
ω	dimensionless vorticity, $\Omega H/V_o$
τ	dimensionless time, tV_o/H

Subscripts

w	solid wall
f	fluid
feff	effective property for the fluid phase
s	solid
seff	effective property for the solid matrix

Symbol

$\langle\ \rangle$	volume-averaged quantity

substrate can substantially enhance the thermal performance of an external boundary. Hwang and Chao [3] investigated experimentally the thermal performance of a porous channel. The results illustrated that the thermal enhancement could be obtained by using a high thermal conductivity porous medium. Recently, Zhang et al. [4] performed a numerical study on the enhancement of combined convective and radiative heat transfer using a porous core in a circular duct. Their results showed that the insertion of the porous material in a circular duct will not only increase the heat transfer by convection, but also enhances the heat transfer by radiation. Porous inserts continue to be an attractive choice in heat transfer augmentation.

Another important aspect in flow through porous media is mixing and recirculation of local fluid streams, which have a significant effect on the transport processes in porous media. This phenomenon is referred to as dispersion. Hunt and Tien [5] discussed the impact of thermal dispersion on the overall heat transfer for natural convection in porous media. Their results showed a significant increase in the average Nusselt number when incorporating thermal dispersion effects.

Most of the studies related to transport in porous media assume that the fluid and the solid exist locally under local thermal equilibrium condition (LTE). This assumption cannot be imposed when there is a significant temperature difference between the fluid and solid phases. Hence, separate energy equations should be used for each phase. Recently, Amiri and Vafai [6] conducted a comprehensive study of the influence of the dispersion, non-thermal equilibrium, non-Darcian, and porosity variation effects on the transport processes in porous media. Comprehensive error maps were presented in this work to show the validity of the local thermal equilibrium concept under various conditions.

In some applications such as electronic devices, a surface is subjected to a high heat flux creating temperature variations along the surface. In various applications, it is required to maintain a surface at a constant temperature. In the present work, a basic and innovative approach is utilized to produce and regulate the surface temperature of an electronic device. This is done through the use of properly setup variable area channel filled with a porous medium. In the present research, a generalized flow model (also known as the Brinkman–Forchheimer–extended Darcy model) has been employed to incorporate the viscous and inertial effects. A two-dimensional transient formulation (vorticity–temperature-stream function) is used to model the flow and

heat transfer processes within the channel. The thermal field is characterized using the local thermal non-equilibrium as well as the LTE models.

2. Problem formulation

The two basic physical models considered in this investigation are shown in Fig. 1. A two-dimensional enclosure is filled with a porous medium of uniform porosity and permeability. The porous medium is assumed to be isotropic and saturated with a fluid. The flow is assumed to be incompressible, and the fluid physical properties are assumed constant except for the density variation in the body force term in the momentum equation where the Boussinesq approximation is invoked. The geometrical attributes of the two basic configurations are given in Fig. 1.

The governing equations, expressed in non-dimensional form, can be written as

$$\omega = -\left(\frac{\partial^2 \Psi}{\partial X^2} + \frac{\partial^2 \Psi}{\partial Y^2}\right), \tag{1}$$

$$U = \frac{\partial \Psi}{\partial Y}, \quad V = \frac{-\partial \Psi}{\partial X}, \tag{2}$$

$$\varepsilon \frac{\partial \omega}{\partial \tau} + U\frac{\partial \omega}{\partial X} + V\frac{\partial \omega}{\partial Y} = \frac{\varepsilon}{Re}\left(\frac{\partial^2 \omega}{\partial X^2} + \frac{\partial^2 \omega}{\partial Y^2}\right) - \frac{\varepsilon^2}{Da\,Re}\omega - \frac{F\varepsilon^2}{\sqrt{Da}}|V|\omega + \frac{F\varepsilon^2}{\sqrt{Da}}\left(U\frac{\partial |V|}{\partial Y} - V\frac{\partial |V|}{\partial X}\right) + \varepsilon^2 \frac{Gr}{Re^2}\frac{\partial \theta}{\partial X}, \tag{3}$$

$$\varepsilon \frac{\partial \theta}{\partial \tau} + U\frac{\partial \theta}{\partial X} + V\frac{\partial \theta}{\partial Y} = \frac{1}{Re\,Pr}\left(\frac{\partial^2 \theta}{\partial X^2} + \frac{\partial^2 \theta}{\partial Y^2}\right) \tag{4}$$

and the energy equation for the solid wall:

$$\frac{\partial^2 \theta_w}{\partial X^2} + \frac{\partial^2 \theta_w}{\partial Y^2} = 0, \tag{5}$$

where $Re = V_o H/\nu_e$, $Da = K/H^2$ and $Pr = \nu_e/\alpha_e$ are the Reynolds number, Darcy number and Prandtl number, respectively. The geometric function F and the permeability of a porous medium K are based on Ergun's model [7] and are expressed as in Vafai [8]:

$$F = \frac{1.75}{\sqrt{150\varepsilon^3}}, \tag{6}$$

$$K = \frac{\varepsilon^3 d_p^2}{150(1-\varepsilon)^2}, \tag{7}$$

where d_p is the particle diameter. The physical configurations for the above system of equations are shown in Fig. 1.

The energy equations for the thermal non-equilibrium model can be written as in Amiri and Vafai [6,9].

(i) *Fluid phase*:

$$\varepsilon \frac{\partial \theta}{\partial \tau} + U\frac{\partial \theta}{\partial X} + V\frac{\partial \theta}{\partial Y} = \frac{1}{Re\,Pr}\left(k_{feff,x}\frac{\partial^2 \theta}{\partial X^2} + k_{feff,y}\frac{\partial^2 \theta}{\partial Y^2}\right) + \frac{1}{Re\,Pr}\left(\frac{\partial k_{feff,x}}{\partial X}\frac{\partial \theta}{\partial X} + \frac{\partial k_{feff,y}}{\partial Y}\frac{\partial \theta}{\partial Y}\right) + \mathscr{R}_1(\Theta - \theta). \tag{8}$$

(ii) *Solid phase*:

$$0 = K_{seff}\left(\frac{\partial^2 \Theta}{\partial X^2} + \frac{\partial^2 \Theta}{\partial Y^2}\right) - \mathscr{R}_2(\Theta - \theta), \tag{9}$$

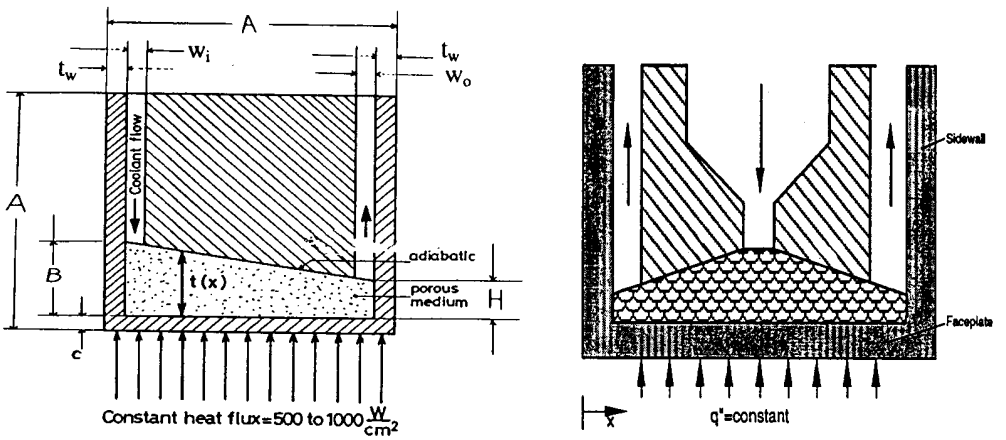

variable area channel configuration symmetric configuration

Fig. 1. Schematic diagram of the present investigation.

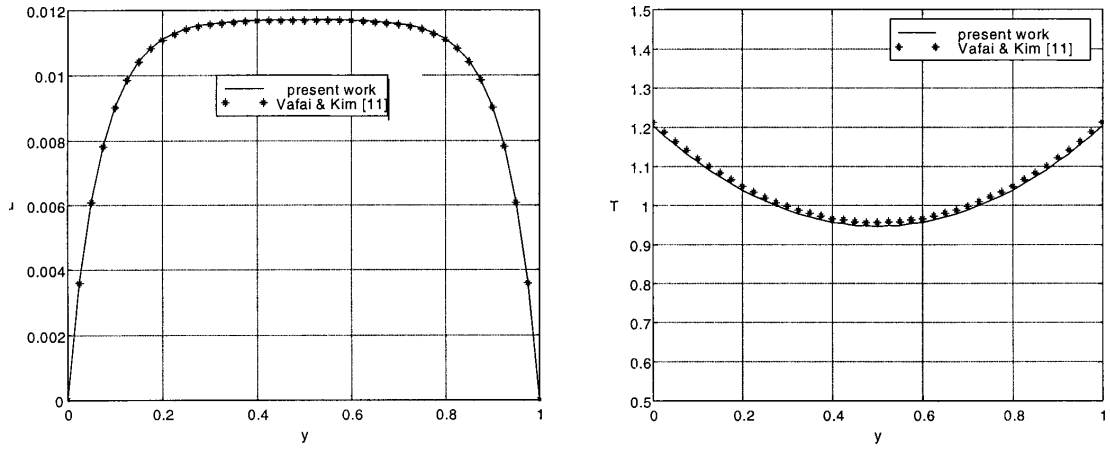

Fig. 2. Comparison of the velocity and temperature profiles between the generalized model and the exact solution for the fully developed flow in a channel [11].

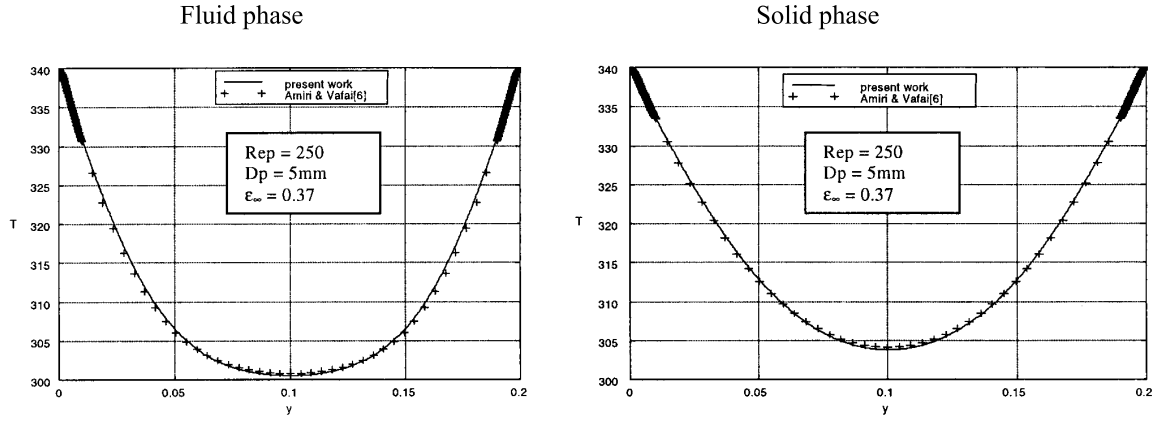

Fig. 3. Comparison of the fluid and solid phases temperature profiles at the mid-section of the channel between the present results and those of Amiri and Vafai [6].

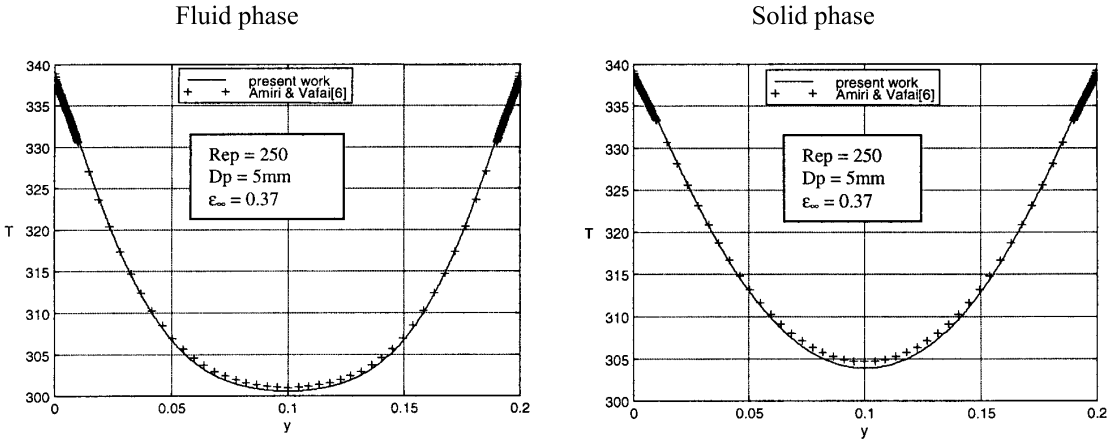

Fig. 4. Comparison of the fluid and solid phases temperature profiles at the exit section of the channel between the present results and those of Amiri and Vafai [6].

where

$$\mathscr{R}_1 = \frac{6(1-\varepsilon)(H/d_p)^2}{Re\,Pr}\left(2 + 1.1Pr^{1/3}\left[\frac{|V|d_p}{\nu_f}\right]^{0.6}\right), \quad (10)$$

$$\mathscr{R}_2 = 6(1-\varepsilon)\left(H/d_p\right)^2\left(2 + 1.1Pr^{1/3}\left[\frac{|V|d_p}{\nu_f}\right]^{0.6}\right). \quad (11)$$

In the above equations, the non-dimensional coordinates X and Y are given by $(x, y)/H$.

2.1. Solution algorithm

The coupled differential equations (1)–(5) and (8)–(11) are first transformed using an algebraic grid transformation to take into account the effect of the inclination and then solved along with the initial and boundary conditions. A uniform transformed orthogonal grid is generated on the computational domain. The transient form of the vorticity transport and the energy equations are solved in the transformed domain using a finite-volume technique, namely, the power-law method [10]. Central differencing scheme was employed for all the derivatives in the corresponding source terms. The unsteady equations are solved using alternating direct implicit algorithm (ADI). The application of the ADI procedure improves the accuracy of the solution since it allows the power-law scheme to be applied locally in an one-dimensional fashion for each sweep in each coordinate direction. When steady-state results were desired, false transient approach was adopted to expedite the convergence toward steady-state conditions. The stream function and the conjugate wall energy equations were

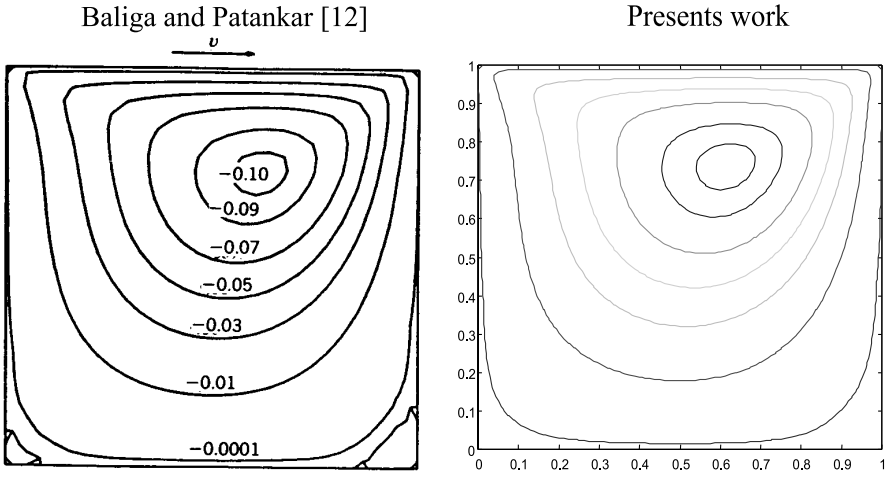

Fig. 5. Comparison of the driven cavity stream function between the present method and that of Baliga and Patankar [12] for $Re = 100$.

Table 1
Primary vortex stream function value

Re	ψ (Present work)	ψ [13]	ψ [14]	ψ [15]
100	−0.10330	−0.10330	−0.10330	−0.103423
400	−0.11390	−0.11389	−0.11297	−0.113909

Table 2
Parametric and geometric variations used in the present investigation

Heat flux q_w (W/cm^2)	Flow rate Q (l/min)	Inlet/outlet width (w_i, w_o) (in.)	Porous		Metal		Flow length A (cm)	Porous metal thickness H (in.)
			d_p (in.)	Porosity	Material	k_s		
500–1000	1.0–4.0	0.03–0.06	0.017–0.04	0.45	Copper	90 W/m K	1.0, 0.5, 0.25	$3.0d_p$

Table 3
Cases to be investigated for various parameters ($T_i = 25°C,\ \Delta T = 50°C$)

Case	Flow rate (l/min)	Inlet/ outlet width (cm)	Particle diameter (cm)	Porosity	Flow length (cm)	Minimum porous matrix thickness (cm)	Heat flux (W/m^2)	Inlet velocity (m/s)	Reynolds number	Permeability (m^2)	Darcy number (Da)	Aspect ratio (AR)	Angle	Inlet pressure (Psi)	Pressure drop (Psi)
Base	1	0.0762	0.04318	0.45	1	0.12954	5.0E+06	2.19	3169.28	3.74E−10	2.231E−04	7.7	0.0	54.11	23.74
Case 1	1	0.0762	0.04318	0.45	1	0.12954	5.0E+06	2.19	3169.28	3.74E−10	2.231E−04	7.7	2.0	60.34	21.76
Case 2	1	0.0762	0.04318	0.45	1	0.12954	5.0E+06	2.19	3169.28	3.74E−10	2.231E−04	7.7	3.0	62.08	20.98
Case 3	1	0.0762	0.04318	0.45	1	0.12954	5.0E+06	2.19	3169.28	3.74E−10	2.231E−04	7.7	4.0	63.66	20.28
Case 4	2	0.0762	0.04318	0.45	1	0.12954	5.0E+06	4.37	6338.55	3.74E−10	2.231E−04	7.7	4.0	241.01	76.42
Case 5	4	0.0762	0.04318	0.45	1	0.12954	5.0E+06	8.75	12,677.11	3.74E−10	2.231E−04	7.7	4.0	949.67	298.57
Case 6	1	0.1016	0.04318	0.45	1	0.12954	5.0E+06	1.64	2376.96	3.74E−10	2.231E−04	7.7	4.0	34.86	10.40
Case 7	1	0.1524	0.04318	0.45	1	0.12954	5.0E+06	1.09	1584.64	3.74E−10	2.231E−04	7.7	4.0	19.53	5.53
Case 8	1	0.0762	0.0508	0.45	1	0.12954	5.0E+06	2.19	3169.28	5.18E−10	3.088E−04	7.7	4.0	28.94	7.77
Case 9	1	0.0762	0.1016	0.45	1	0.12954	5.0E+06	2.19	3169.28	2.07E−09	1.235E−03	7.7	4.0	27.88	7.29
Case 10	1	0.0762	0.04318	0.45	0.5	0.12954	5.0E+06	2.19	3169.28	3.74E−10	2.231E−04	3.9	4.0	58.47	7.37
Case 11	1	0.0762	0.04318	0.45	0.25	0.12954	5.0E+06	2.19	3169.28	3.74E−10	2.231E−04	1.9	4.0	49.50	2.88
Case 12	1	0.0762	0.04318	0.45	1	0.25908	5.0E+06	2.19	6338.55	3.74E−10	5.579E−05	3.9	4.0	111.34	15.08
Case 13	1	0.0762	0.04318	0.45	1	0.38862	5.0E+06	2.19	9507.83	3.74E−10	2.479E−05	2.6	4.0	149.47	13.37
Case 14	1	0.0762	0.04318	0.45	1	0.12954	7.5E+06	2.19	3169.28	3.74E−10	2.231E−04	7.7	4.0	63.67	20.15
Case 15	1	0.0762	0.04318	0.45	1	0.12954	1.0E+07	2.19	3169.28	3.74E−10	2.231E−04	7.7	4.0	63.67	20.15
Symmetric configuration															
Base	1	0.0762	0.04318	0.45	1	0.12954	5.0E+06	2.19	3169.28	3.74E−10	2.231E−04	3.9	0	113.07	26.20
Case 16	1	0.0762	0.04318	0.45	1	0.12954	5.0E+06	2.19	3169.28	3.74E−10	2.231E−04	3.9	2	119.41	25.73
Case 17	1	0.0762	0.04318	0.45	1	0.12954	5.0E+06	2.19	3169.28	3.74E−10	2.231E−04	3.9	4	123.62	25.33
Case 18	1	0.0762	0.04318	0.45	1	0.12954	5.0E+06	2.19	3169.28	3.74E−10	2.231E−04	3.9	5	125.71	25.16
Case 19	1	0.0762	0.04318	0.45	1	0.12954	5.0E+06	2.19	3169.28	3.74E−10	2.231E−04	3.9	6	129.92	25.64

discretized using an iterative scheme, namely, successive over relaxation method (SOR).

Vorticity–stream function formulation does not include the pressure term. Therefore, the velocity field is determined initially, and subsequently, the Poisson equation for the pressure is employed to solve for the pressure field. The transformed Poisson equation is discretized using an iterative finite-difference scheme, namely, successive over relaxation method (SOR). All the derivatives are discretized using a central finite difference scheme. The pressure at the surface is not known and must be determined as a part of the solution. For this reason, the Neumann type boundary condition is imposed for the pressure. For this purpose, a relation involving the normal pressure gradient is obtained from the appropriate momentum equation.

An algebraic grid generation technique was employed to transform the variable area domains for the basic configurations shown in Fig. 1 into a rectangular domain. The major advantage of this scheme is the speed with which a grid can be generated. An algebraic equation is used to relate the grid points in the computational domain to those of the physical domain. With the use of an algebraic model, the metrics and the Jacobian of the transformation are calculated analytically. This aspect is obviously an advantage of the algebraic method, since numerical computation of the metrics will require additional computation time and may introduce some errors into the system of equations, which are to be solved. The y coordinate is transformed to an η coordinate through a transformation prescribed by $\eta = y/y_o; y_o = H - (x - L)\tan\varphi$, where H is the minimum porous

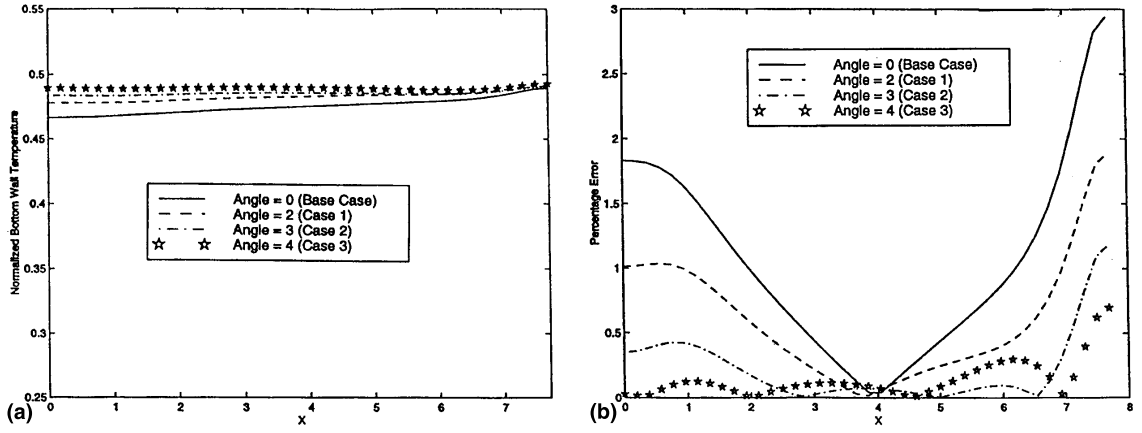

Fig. 6. Effect of the inclination angle of the enclosure top surface of the base case on: (a) normalized bottom wall temperature; (b) percentage error.

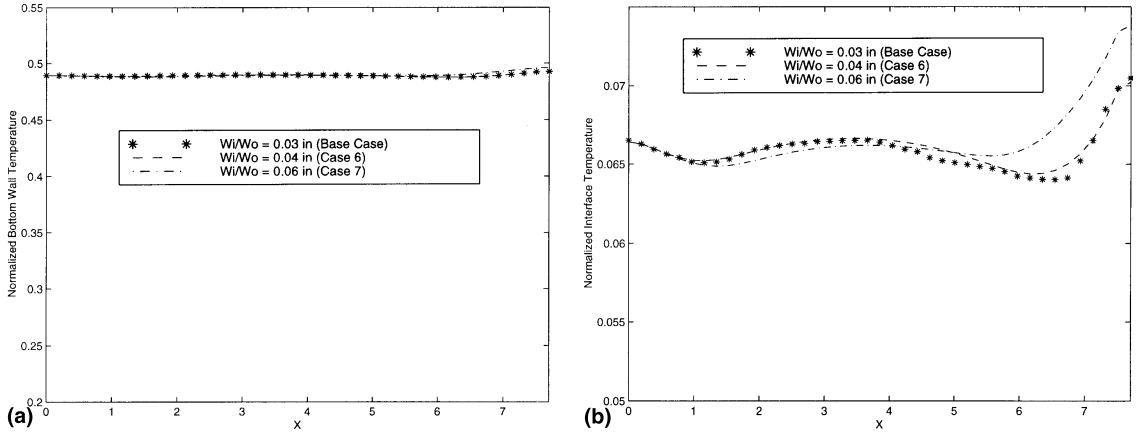

Fig. 7. Effect of the inlet/outlet width on: (a) normalized bottom wall temperature; (b) normalized bottom interface temperature of the porous substrate.

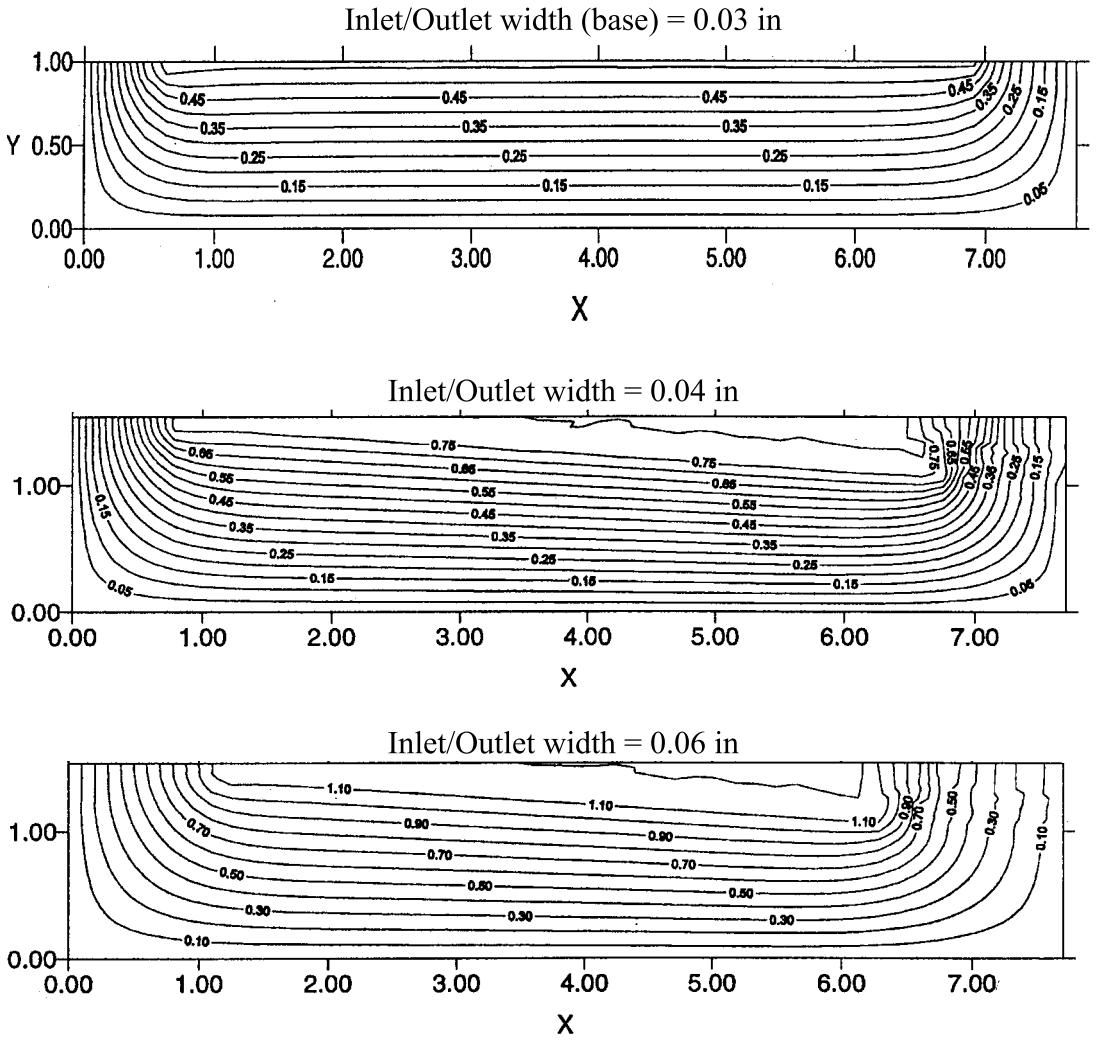

Fig. 8. Effect of the inlet/outlet width variation on the streamlines.

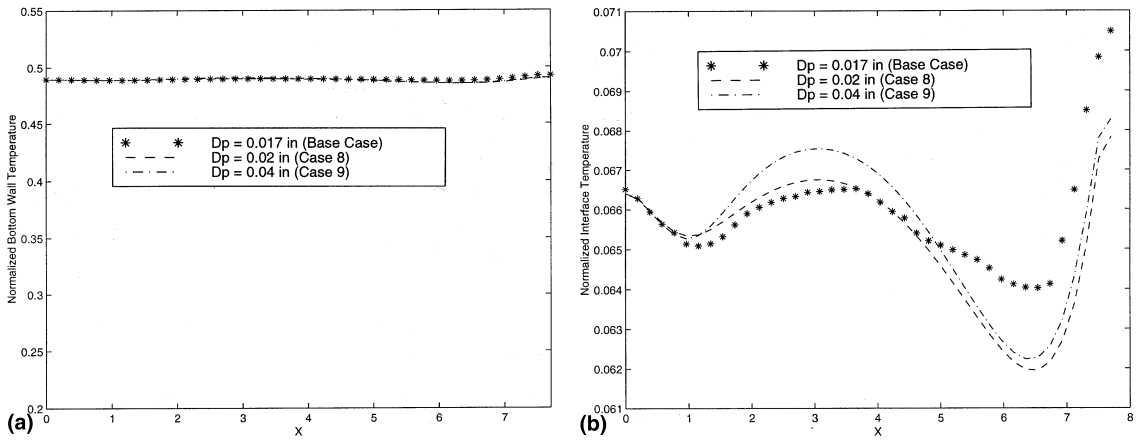

Fig. 9. Effect of the particle diameter on: (a) normalized bottom wall temperature; (b) normalized bottom interface temperature of the porous substrate.

thickness, L the flow length, and φ is the inclination angle of the top surface. The x coordinate is transformed such that $\xi = x$. The boundary conditions for the vorticity and heat fluxes on the walls are then transformed using the above general transformed relations. The vortcity on the walls is calculated using the following equation:

$$\omega = \frac{\partial V}{\partial X} - \frac{\partial U}{\partial Y} = \frac{\partial V}{\partial \xi} + \frac{\eta \tan \varphi}{y_o}\frac{\partial V}{\partial \eta} - \frac{1}{y_o}\frac{\partial U}{\partial \eta}. \quad (12)$$

The heat flux on the walls is calculated in the same manner.

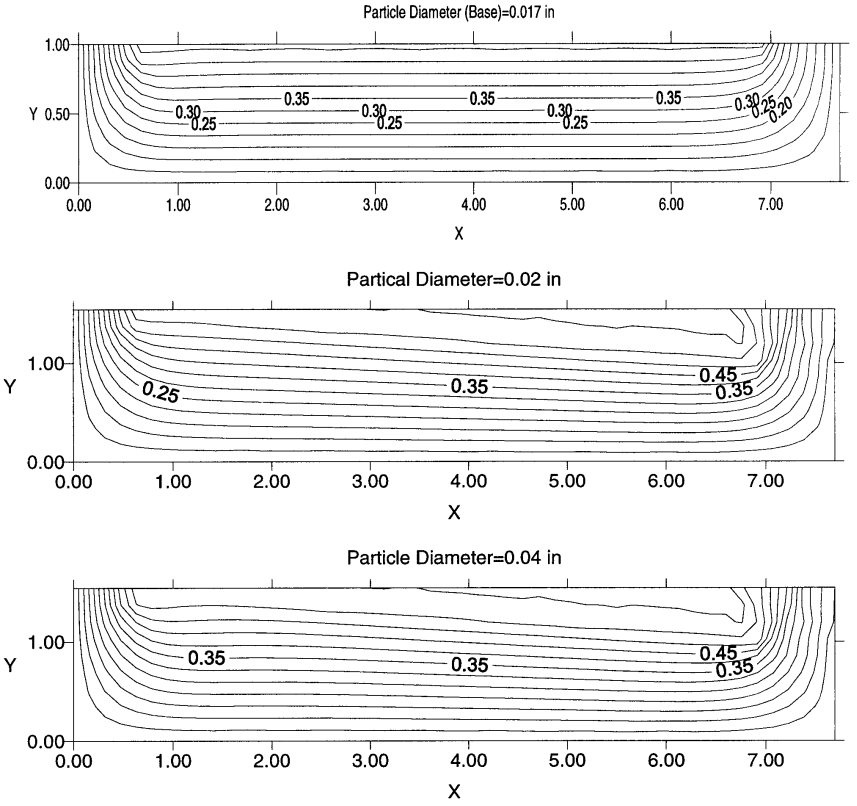

Fig. 10. Effect of the particle diameter on the streamlines.

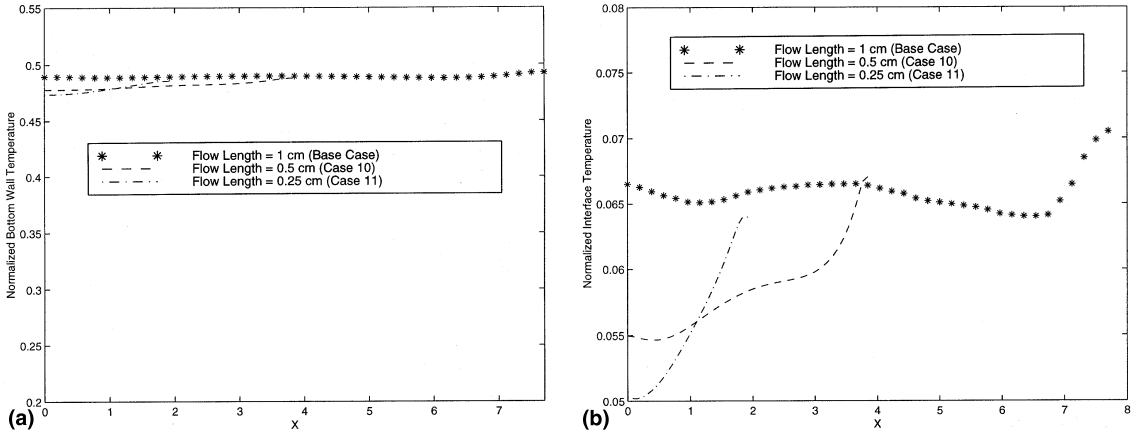

Fig. 11. Effect of the flow length on: (a) normalized bottom wall temperature; (b) normalized bottom interface temperature of the porous substrate.

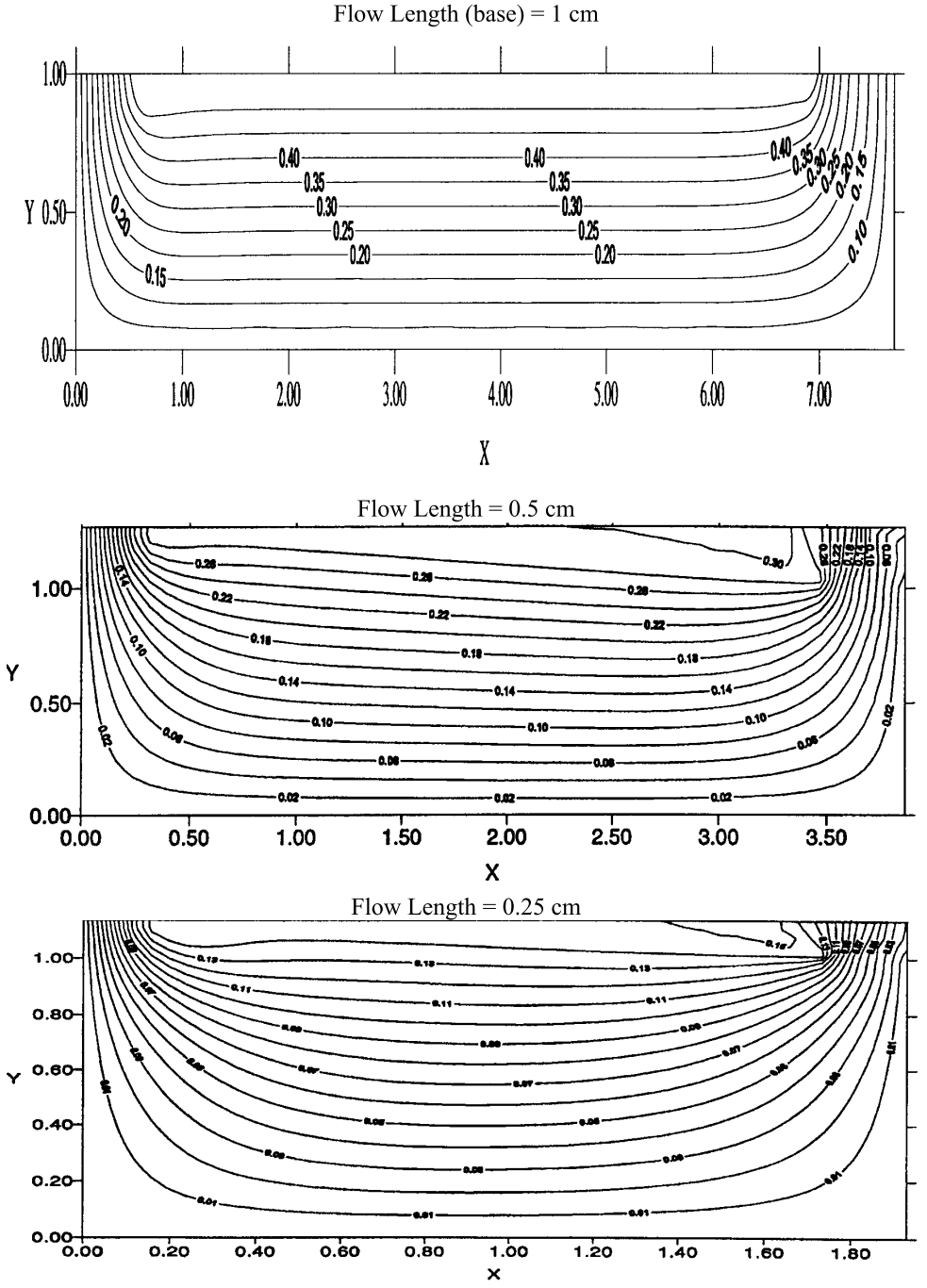

Fig. 12. Effect of the flow length on the streamlines.

2.2. Model validation

Extensive numerical experimentation was performed to establish grid independence results. It was found that an equally spaced grid mesh of 41×41 provides grid independence results. Further increase in the number of grid points produced, essentially the same results. The following criterion was employed to assess convergence of the steady-state solution

$$\Delta = \frac{\left\|\Omega^{n+1} - \Omega^{n}\right\|_{\infty}}{\left\|\Omega^{n+1}\right\|_{\infty}} + \frac{\left\|\theta^{n+1} - \theta^{n}\right\|_{\infty}}{\left\|\theta^{n+1}\right\|_{\infty}} \leqslant 10^{-6}, \tag{13}$$

where the operator $\| \quad \|_\infty$ indicates the maximum absolute value of the variable over all the grid points in the computational domain.

Benchmarking of the present code is considered to be an important part of this work. As such, results obtained from the code developed for the present investigation have been compared against three different and well established physical categories. These are forced convection through a constant porosity medium, forced convective incompressible flow through a variable porosity medium, and the driven cavity problem.

2.2.1. Forced convection through a constant porosity medium

The present generalized model is validated by comparing the velocity and temperature profiles at the mid-section of a channel filled with a porous medium with that of Vafai and Kim [11]. In order to reproduce the results of the channel flow problem, the aspect ratio of the enclosure is taken to be large; i.e., a shallow enclosure, to ensure a fully developed flow within the core region. Fig. 2 presents a comparison of the velocity and temperature profiles between the two-dimensional solution inside the enclosure and the exact solution of Vafai and Kim [11] inside a channel for Reynolds number, $Re = 100$ and Darcy number, $Da = 10^{-3}$. As seen in Fig. 2, there is an excellent agreement between the present work and the exact solution presented in [11].

2.2.2. Forced convective incompressible flow through a variable porosity medium

Next, comparisons for forced convective flow and heat transfer through a variable porosity media were carried out. A general model for the momentum equation was employed. The energy equation was based on the two-phase equation model to account for non-local thermal equilibrium between the fluid and the solid phases. The effects of dispersion, non-Darcian, and variable porosity medium were taken into consideration. The results of the present model were validated against the results given in [6]. A sample of these comparisons for the fluid and solid phases temperature profiles at two different locations in the channel, for particle Reynolds number, $Re_p = 250$, particles diameter $d_p = 5$ mm, and the asymptotic free stream porosity of $\epsilon_\infty = 0.37$, are shown in Figs. 3 and 4. As can be seen from these figures, there is an excellent agreement between the present work and that of Amiri and Vafai [6].

2.2.3. Driven cavity problem

The driven cavity problem is used here to verify the circulating nature of the present configuration. The results for the driven cavity problem with a non-dimensionalized unit lid, velocity are simulated in this part. The boundary conditions are $\psi = 0$, $v = 0$ and $u = 0$ on all boundaries except at the lid where $u = 1$. The results were compared with the finite-difference solution of Baliga and Patankar [12] in the absence of the porous medium as shown in Fig. 5. This comparison revealed excellent agreement between the two numerical solutions. In addition, Table 1 shows a comparison of the stream function values at the primary vortex location computed for various Reynolds numbers between the present work and several other numerical solutions. The agreement between the present and other work is remarkably good.

3. Results and discussion

3.1. Variable area channel configuration

A range of heat flux, flow rate specifications, and geometric variations relevant to practical applications

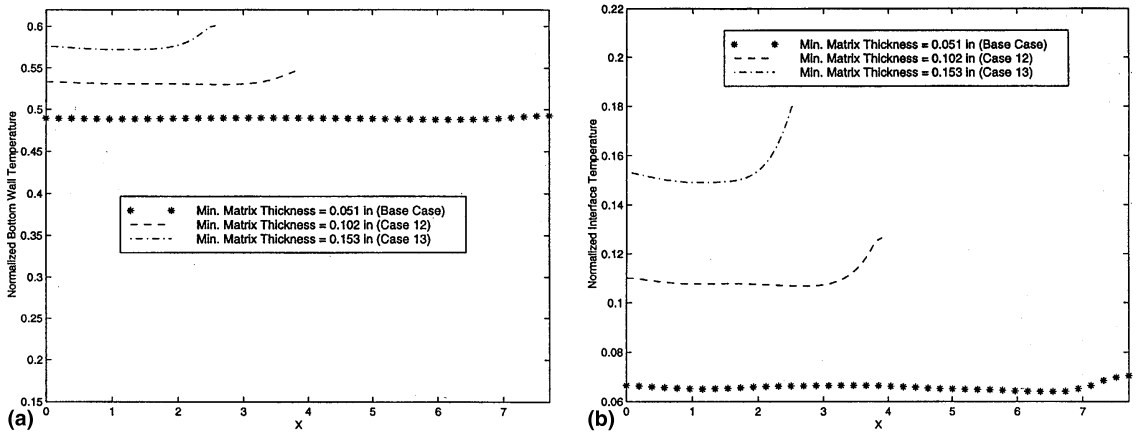

Fig. 13. Effect of the minimum matrix thickness on: (a) normalized bottom wall temperature; (b) normalized bottom interface temperature of the porous substrate.

were utilized in the present investigation. These values are shown in Table 2. Detailed specifications of the illustrative cases that have been presented are shown in Table 3. The presented cases are a subset of a much larger comprehensive investigation of variations in various configuration and geometric parameters. A base case is selected on the basis of practical operating conditions. The inclination angle of the top surface is then varied until constant temperature variation along the bottom wall is approximately achieved as shown in

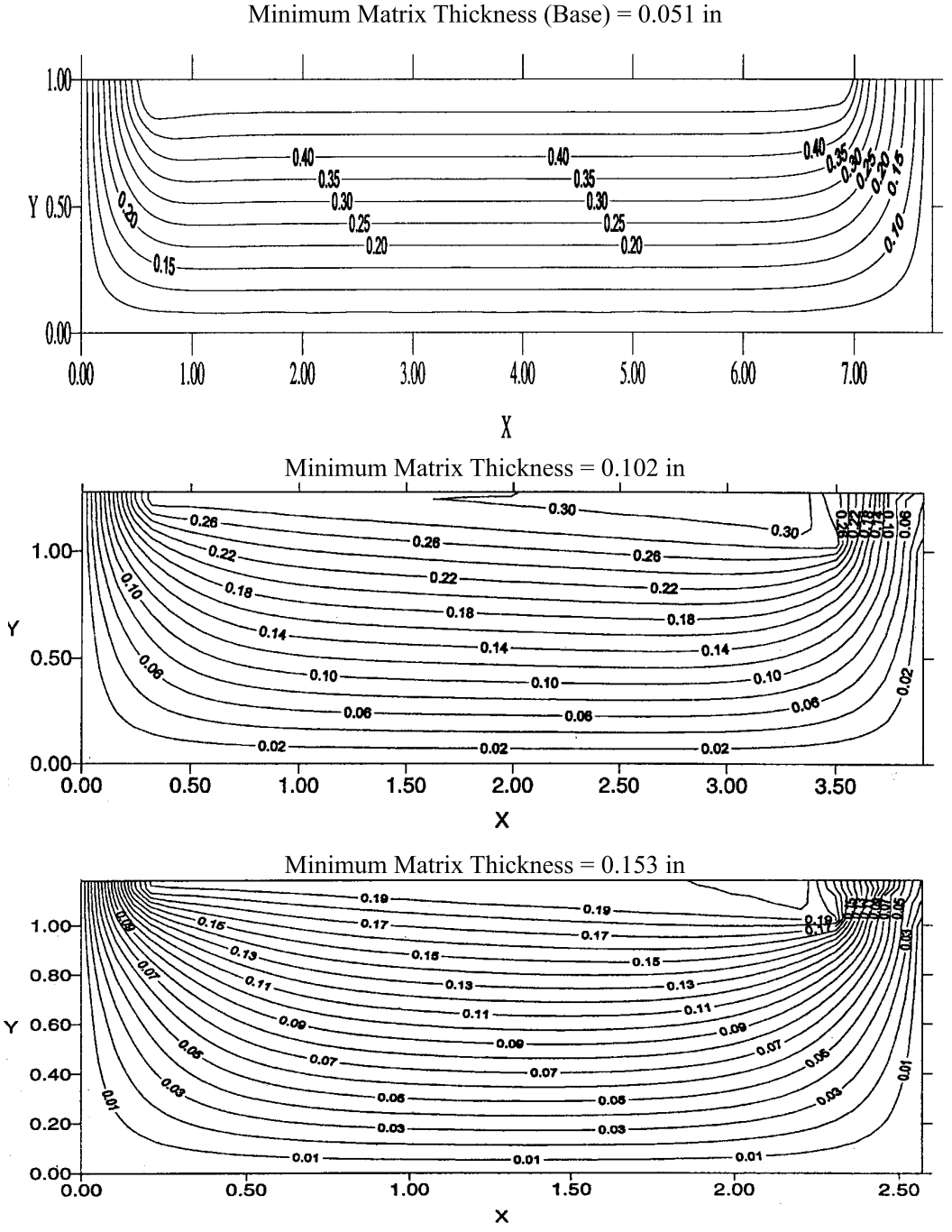

Fig. 14. Effect of the minimum matrix thickness on the streamlines.

Figs. 6(a) and (b). These figures show that for an angle of 4° the temperature distribution is almost constant. It is seen in Fig. 6(b) that the percentage error based on the average temperature, is well under 1% for an angle of 4°. The realized optimum angle based on cases 1–4 is used for other cases (case 4–15) to illustrate the effect of various other pertinent parameters on the temperature distribution along the top and bottom walls, and the streamlines.

Fig. 7 illustrates the effect of the inlet/outlet width on the normalized temperature distributions along the bottom interface of the variable area porous substrate as well as the bottom wall for the optimum inclination angle. It can be seen from this figure that the temperature distribution along the bottom wall is almost constant for various inlet/outlet widths. This is due to the variable area configuration and the selection of the optimum angle, which gives almost constant temperature distribution along the bottom wall surface. As the inlet/outlet width increases, while the flow rate remains the same, the rate of cooling decreases (lower inlet velocity) and higher temperature region is found at the exit port of the enclosure. The effect of inlet/outlet width variation on the streamlines is shown in Fig. 8. For the base case, the core region can be described as a fully developed flow region except at the ports where the two-dimensional nature of the flow is more pronounced. Therefore, for the base case, a one-dimensional model can approximate the flow in the core region. As the inclination angle for the top surface increases, it causes a tilt in the streamlines as seen in Fig. 8. Moreover, the flow is not fully developed anymore except near the bottom surface of the enclosure where the flow can still be considered as fully developed.

The effect of the particle diameter size on the temperature distribution along the bottom interface of the porous substrate and the bottom solid wall is shown in Fig. 9. The temperature distribution along the bottom wall is nearly constant for different particle diameters as depicted in Fig. 9. However, the effect of changing the particle diameter on the normalized interface temperature is significant near the exit port as seen in Fig. 9. This can be attributed to the lower cooling rate at the exit port for the smaller particle diameters, which results in lower exit velocities. The influence of particle diameter variation on the streamlines as compared with the baseline case is shown in Fig. 10. The presence of a porous medium within the cavity results in a force opposite to the flow direction, which tends to resist the flow. As expected, as the Darcy number increases (increasing the particle diameter) the resistance of the solid matrix to the flow decreases.

Fig. 11 shows the effect of flow length variation on the bottom porous interface and the bottom solid wall temperature distributions. It can be seen from Fig. 11 that the bottom wall temperature is more uniform for longer flow lengths. This effect is more significant at smaller aspect ratios as can be seen from the streamline contours shown in Fig. 12. As the flow length decreases, the core region is no longer fully developed and the two-dimensional nature of the flow becomes more prominent through the entire enclosure. Moreover, the intensity of the streamlines at the inlet port of the enclosure decreases as the flow length decreases.

Fig. 13 illustrates the influence of the minimum matrix thickness on the temperature distribution along the top and bottom of the base wall. It can be seen from Fig. 13 that the bottom wall temperature distribution is nearly constant throughout the bottom wall surface except near the right side wall of the enclosure. This is due to the two dimensional nature of the flow which becomes more significant for larger minimum matrix thickness as seen in Fig. 14.

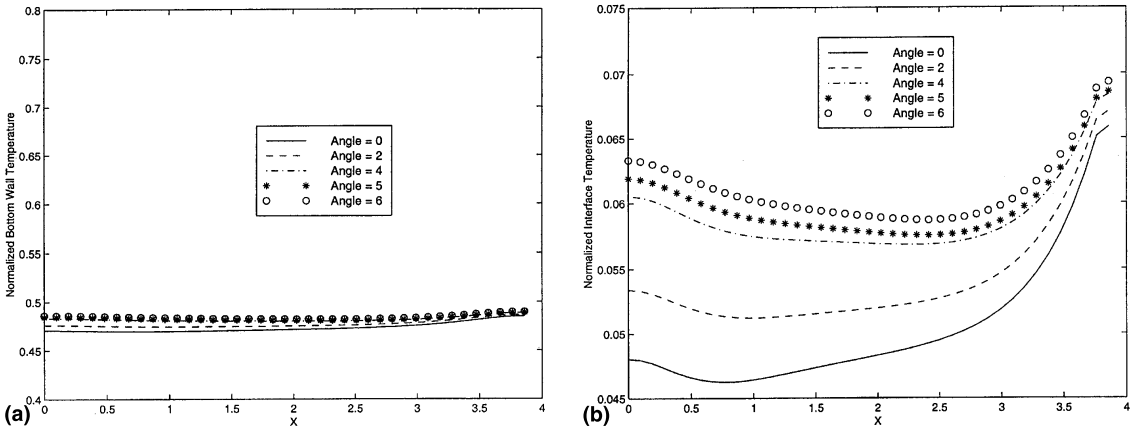

Fig. 15. Effect of the inclination angle of the enclosure top surface of the symmetric case on: (a) normalized bottom wall temperature; (b) normalized bottom interface temperature of the porous substrate.

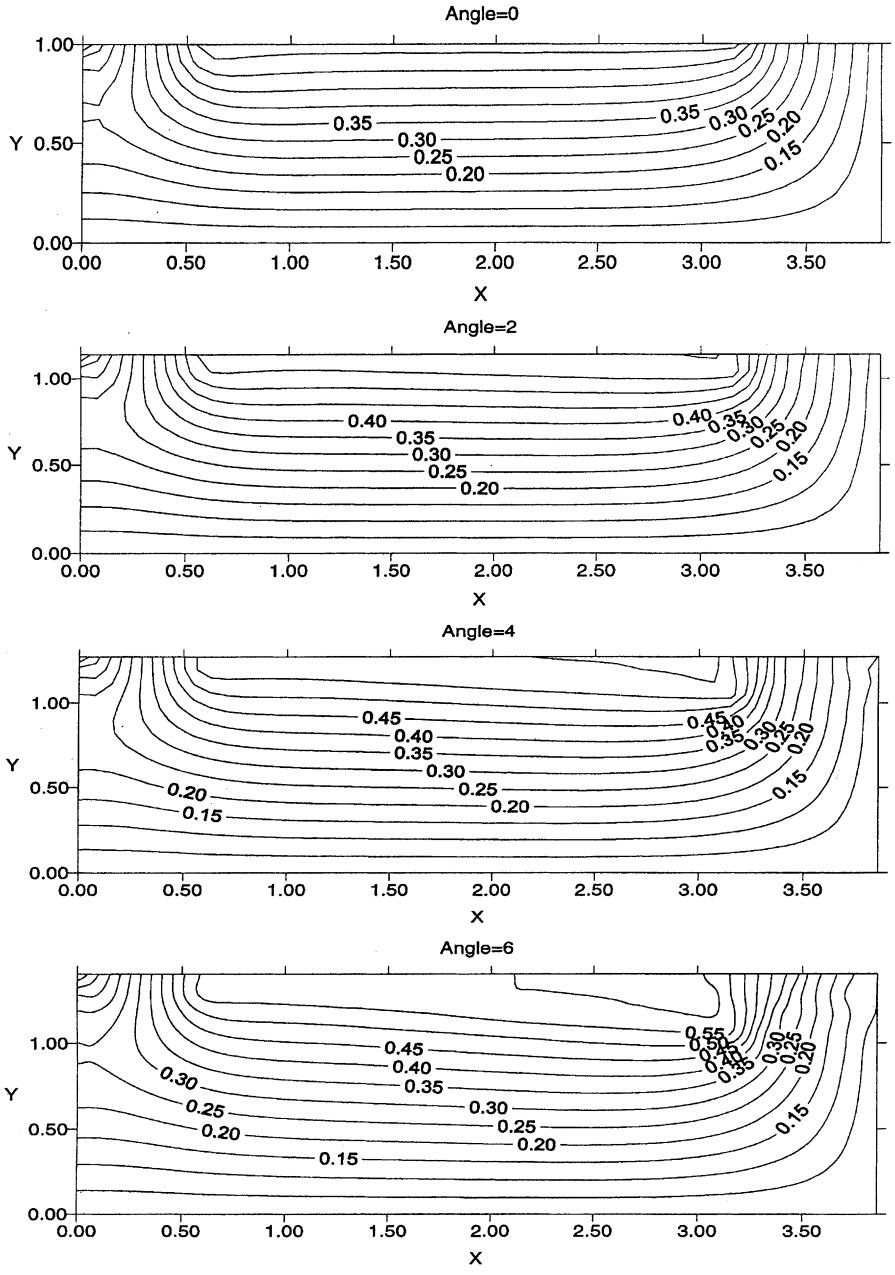

Fig. 16. Effect of the inclination angle of the top surface on the streamlines.

3.2. Symmetric configuration

For the symmetric configuration, the inclination angle of the top surface is varied from 0° to 6° until an almost constant temperature distribution is obtained along the bottom surface wall as shown in Fig. 15. It can be seen from Fig. 15 that again an angle 4° to 5° results in an almost constant temperature along the bottom wall. The effect of the inclination angle on the interface temperature is more pronounced at higher inclination angles as shown in Fig. 15(a). Fig. 16 shows the effect of the inclination angle variation on the streamline contours for the symmetric configuration. The two-dimensional effects at the ports can be clearly seen in this figure.

It should be noted that comparisons of the results using the LTE and non-thermal equilibrium models indicate that the non-LTE model has a slight effect on the

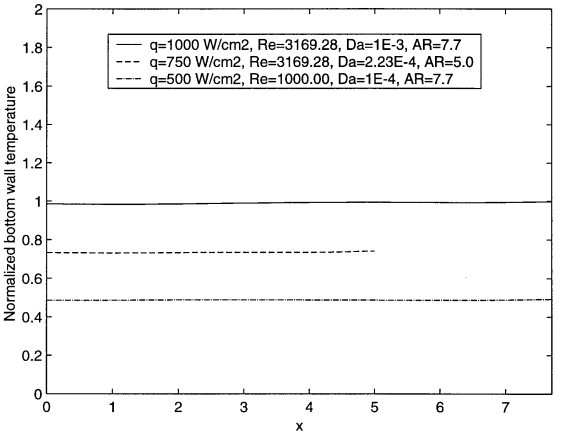

Fig. 17. Effect of the optimum angle of the variable area channel configuration on the normalized bottom wall temperature for various pertinent parameters.

optimum inclination angle. As such, LTE model can be used in predicting the optimum angle.

3.3. Optimum angle for producing an isothermal surface of the variable area channel configuration

The optimum angles for producing isothermal surfaces along the bottom wall of a variable channel configuration are obtained for various pertinent controlling parameters such as Reynolds number, aspect ratio, Darcy number, and the applied heat flux. The controlling parameters covered by that optimum angles are $500 \leqslant q(\mathrm{W/cm^2}) \leqslant 1000$, $10^3 \leqslant Re \leqslant 10^4$, $1.5 \leqslant \mathrm{AR} \leqslant 7.7$ and $10^{-3} \leqslant \mathrm{Da} \leqslant 10^{-6}$. Few examples, related to the applicability of that optimum angles are shown in Fig. 17. This optimum angle prescribes the geometrical configuration required to obtain almost constant bottom wall temperature for the specified range of controlling parameters.

4. Conclusions

In this work, a fundamental methodology for production and regulation of an isothermal surface using porous inserts was presented. A comprehensive investigation of variable area distribution of the porous inserts in producing the constant surface temperature was performed. This technique is promising for various applications especially those characterized by large heat flux.

Acknowledgements

The grant from Thermacore Corporation is acknowledged and appreciated.

References

[1] K. Vafai, P.C. Huang, Analysis of heat transfer regulation intermittently emplaced porous cavities, ASME J. Heat Transfer 116 (1994) 155–164.
[2] K. Vafai, S.J. Kim, Analysis of surface enhancement by a porous substrate, ASME J. Heat Transfer 112 (1990) 700–706.
[3] G.J. Hwang, C.H. Chao, Heat transfer measurement and analysis enhancement for sintered porous channels, Heat and Mass Transfer in Porous Media HTD 216 (1992) 19–26.
[4] J.M. Zhang, W.H. Sutton, F.C. Lai, Enhancement of heat transfer using porous convection-to-radiation covertor for laminar flow in a circular duct, Int. J. Heat Mass Transfer 40 (1) (1997) 39–48.
[5] M.L. Hunt, C.L. Tien, Non-Darcian convection in cylindrical packed beds, ASME J. Heat Transfer 110 (1988) 2523–2532.
[6] A. Amiri, K. Vafai, Analysis of dispersion effects and non-thermal equilibrium, non-Darcian, variable porosity incompressible flow through porous media, Int. J. Heat Mass Transfer 37 (6) (1994) 939–954.
[7] S. Ergun, Fluid flow through packed columns, Chem. Engng. Progress 48 (1952) 89–94.
[8] K. Vafai, Convective flow and heat transfer in variable porosity media, J. Fluid Mech. 147 (1984) 233–259.
[9] A. Amiri, K. Vafai, Transient analysis of incompressible flow through a packed bed, Int. J. Heat Mass Transfer 41 (1998) 4259–4279.
[10] S.V. Patankar, Numerical Heat Transfer and Fluid Flow, McGraw-Hill, New York, 1980.
[11] K. Vafai, J. Kim, Forced convection in a channel filled with a porous medium: an exact solution, ASME J. Heat Transfer 111 (1989) 1103–1106.
[12] B.R. Baliga, S.V. Patankar, Elliptic Systems: Finite-element Method, Numerical Heat Transfer, Hemisphere, Washington, DC, 1984.
[13] E. Barragy, G.F. Carey, Stream function–vorticity driven cavity solution using p finite element, Comput. Fluids 26 (5) (1997) 453–468.
[14] R. Screiber, H.B. Keller, Driven cavity flows by efficient numerical techniques, J. Comput. Phys. 49 (1983) 310–333.
[15] U. Ghia, K. Ghia, C. Shin, High *Re* solutions for incompressible flow using the Navier–Stokes equations and multigrid method, J. Comput. Phys. 48 (1982) 387–411.